

# Analysis of Terahertz Waveforms Measured by Photoconductive and Electrooptic Sampling

Sang-Gyu Park, Michael R. Melloch, *Senior Member, IEEE*, and Andrew M. Weiner, *Fellow, IEEE*

**Abstract**—Terahertz (THz) waveform measurements by photoconductive (PC) sampling and free-space electrooptic sampling (FS-EOS) are analyzed and quantitatively compared. Our data suggest that a short dipole antenna used in a PC receiver contributes a flat frequency response when used without a substrate lens and a  $j\omega$  response when used with a substrate lens, for the specific THz frequency range and optical system investigated in our experiments. These findings are explained using results from basic antenna theory. Experiments testing our theory for a variety of THz waveforms (obtained by using different THz emitters and simple as well as shaped optical excitation pulses) and for different carrier lifetimes are also presented. Finally, we demonstrate near-field effects in the PC-sampling measurements of broad-band THz waveforms and explore the evolution of THz radiation from the near field into the far field.

**Index Terms**—Antenna theory, electrooptic sampling, near-field effects, photoconductive sampling, submillimeter-wave measurements, substrate lens, terahertz radiation.

## I. INTRODUCTION

SINCE THE 1980's, coherent terahertz (THz) radiation has been of much interest in the ultrafast optics community [1]–[8]. This THz frequency range, which is in the submillimeter regime in terms of wavelength, had been difficult to reach prior to the application of femtosecond lasers for the generation of coherent THz radiation. When one deals with THz phenomena, waveform measurement is as important as the generation of the phenomena. For the measurement of THz radiation, photoconductive (PC) sampling and free-space electrooptic (EO) sampling are two currently widely used techniques. PC sampling has played an important role in the development of THz technology itself. Because of exceptionally good signal-to-noise ratio (SNR) and reasonable bandwidth, it has enabled many applications, including spectroscopy [9]–[11], imaging [12], [13], and ranging [14]. On the other hand, EO sampling of freely propagating THz radiation is relatively young. Although the EO effect itself has been known for a long time, and EO sampling of guided THz propagation was demonstrated some time ago [15], it was not until recently

that EO sampling of freely propagating THz was demonstrated. Zhang and Wu [16]–[21] and Heinz *et al.* [22], [23] developed free-space electrooptic sampling (FS-EOS) in the mid-1990's. Once the FS-EOS technique was developed, it has become very popular, mainly due to its simple implementation and large bandwidth.

In this paper, we analyze and compare the FS-EOS and PC sampling techniques. We will emphasize the relation between the waveforms measured by these techniques. Although these methods are widely used to measure coherent THz radiation, there are not many works comparing these two methods. The comparison has focused mainly on the bandwidth and the SNR [17], [24], but detailed comparison of the detected waveforms has been missing. In a recent paper [25], we quantitatively compared the THz waveforms measured by FS-EOS and PC sampling and showed that the waveforms measured by FS-EOS and PC sampling could be related by a simple formalism. In this work, we extend the comparison to the case in which the THz waveforms are more complex, and we present a detailed theoretical analysis which explains the observed PC antenna response (which in turn can lead to important differences in the waveforms measured via these two techniques). The effect of the carrier lifetime on the PC-sampled THz waveform is also demonstrated experimentally and compared to theory. Finally, we discuss experiments demonstrating near-field effects and the transition from the near-field to the far-field region for wide-band THz radiation.

## II. THEORY OF FS-EOS AND PC SAMPLING

### A. FS-EOS

In FS-EOS, we detect the polarization change of the probe beam induced by the THz electric field through the EO effect in the sensor crystal. The typical FS-EOS experimental arrangement used in this research is shown in Fig. 1. The THz beam and the optical probe beam copropagate in the EO sensor crystal. The optical probe beam path is provided by a thin pellicle beamsplitter, which has a negligible effect on the THz beam. The linearly polarized probe beam experiences a polarization change in the sensor crystal due to the birefringence induced by the THz electric field. Usually, the sensor crystal is a  $\langle 1\bar{1}0 \rangle$ -oriented zinc-blende crystal which possesses  $\bar{4}3m$  symmetry. When the  $[1\bar{1}0]$  edge of the crystal is oriented parallel to the polarizations of the incoming THz beam and optical probe beam, the differential phase change  $\Gamma$  of the two probe beam polarization components due to the induced

Manuscript received November 2, 1998; revised January 13, 1999. This work was supported by the National Science Foundation under Grant 9404677-PHY and Grant 9722668-PHY. The work of M. R. Melloch was supported by AFOSR under Grant F49620-96-0234A.

S.-G. Park was with the School of Electrical and Computer Engineering, Purdue University, West Lafayette, IN 47907-1285 USA. He is now with AT&T Research, Red Bank, NJ 07701 USA.

M. R. Melloch and A. M. Weiner are with the School of Electrical and Computer Engineering, Purdue University, West Lafayette, IN 47907-1285 USA.

Publisher Item Identifier S 0018-9197(99)03404-1.

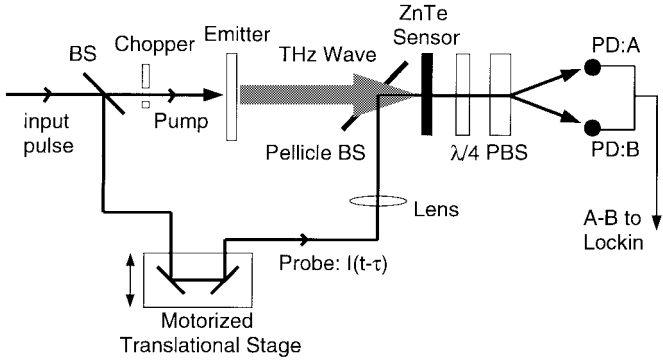


Fig. 1. Setup for FS-EOS of THz waves in a back-to-back configuration. BS: beamsplitter; PD: photodiode; PBS: polarization beamsplitter;  $\lambda/4$ : quarter-wave plate).

birefringence can be expressed by [26]

$$\Gamma(\omega) = \frac{n^3 r_{41} E_{\text{THz}}(\omega) \omega L}{c} \quad (1)$$

where  $n$ ,  $r_{41}$ , and  $L$  are the refractive index, EO coefficient, and thickness of the sensor crystal, respectively.  $E_{\text{THz}}(\omega)$  is the amplitude of the THz electric field,  $\omega$  is the angular frequency of the optical probe beam, and  $c$  is the speed of light. The modulated probe beam is analyzed by a setup which consists of a quarter-wave plate, a polarization beamsplitter and a pair of balanced photodiodes. The detected differential current signal can be expressed by

$$\Delta I = I_0 \sin(\Gamma) \quad (2)$$

where  $I_0$  is the current which would flow in a diode when all the optical probe power is directed to a single diode. For a moderate modulation depth, the phase change is converted linearly to the differential current. (The typical modulation depth is  $10^{-3}$ – $10^{-4}$ .)

There are several factors which can affect EO-sampled waveforms. These include group velocity mismatch (GVM) in the sensor crystal, phonon–polariton coupling, and finite optical pulsewidth [21]. The GVM arises from the different propagation speeds of the THz and optical waves in the sensor crystal; this leads to broadening of the measured waveform. The amount of GVM depends on the wavelength of the probe beam and the type of sensor crystal, but it can be as large as several picoseconds per millimeter of sensor crystal length [17]. The phonon–polariton coupling describes the phenomenon in which the propagating THz wave leaves behind phonon oscillations, which in turn act as a source of THz radiation. The phonon–polariton coupling usually manifests itself as an oscillatory tail accompanying the main THz features [27]. These two effects—GVM and phonon–polariton coupling—can be minimized by using thin sensor crystals at the expense of reduced signal strength. The finite probe beam pulsewidth is another source of THz waveform broadening, which can be significant for very short THz waveforms. However, in our experiments with 100-fs probe pulses, THz radiation with a spectrum under 2–3 THz, and a thin (150  $\mu\text{m}$ ) ZnTe EO sensor crystal, distortion of the THz waveforms by all these effects is minimal. For

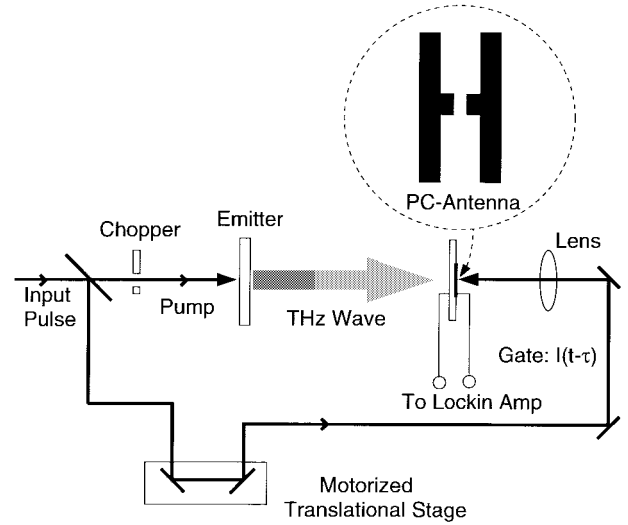


Fig. 2. Setup for PC sampling of THz waves in a back-to-back configuration.

example, the GVM between the optical probe at 810 nm and the THz beam around 1–2 THz for 150  $\mu\text{m}$  ZnTe is 10–20 fs, which is negligible for our frequency range. The effect of phonon–polariton coupling is more difficult to state quantitatively. But, if we compare our conditions with those of [21] and [27], we find it is safe to assume that the phonon–polariton coupling effects are small. Therefore, we consider the measured waveforms to be directly proportional to the incoming THz electric field amplitude. In the context of our comparison with PC sampling, the ability to independently measure the incoming THz field via FS-EOS isolates the role of the antenna frequency response in the PC-sampling measurement.

### B. PC Sampling

In PC sampling, the measured quantity is the current which flows in the photoconductor excited by delayed optical gate pulses. A typical PC-sampling setup is shown in Fig. 2. Electron–hole pairs are generated when an optical gate pulse illuminates the photoconductor in the gap of a dipole antenna. These carriers are driven by the THz electric field, producing a current, the magnitude of which is proportional to the THz field and the carrier concentration and the direction of which is determined by the polarity of the THz field. Since the basic operation principle of a PC antenna is the same as that of an electronic boxcar, a rapid recovery of the electron–hole population is essential in order to get good time resolution. Usually, radiation-damaged silicon-on-sapphire (RD-SOS) [28] or low-temperature-grown GaAs (LT-GaAs) [29]–[31] are used as the photoconductor material. The average photocurrent  $I_{\text{PC}}$  as a function of delay  $\tau$  of the gating pulse can be expressed by the convolution of

$$I_{\text{PC}}(\tau) \equiv \frac{Q(\tau)}{T} = \int dt v_g(t) g(t - \tau) \quad (3)$$

where  $Q(\tau)$  is the collected charge for each gate pulse,  $1/T$  is the repetition rate of the laser, and the induced bias voltage

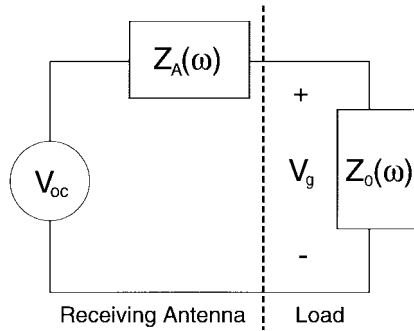


Fig. 3. An equivalent circuit diagram of an antenna in receiving mode.  $Z_0$ : transmission line impedance;  $Z_A$ : antenna impedance;  $V_{oc}$ : induced open-circuit voltage.

across the photoconductive gap  $v_g(t)$  is

$$v_g(t) \sim \int d\omega H(\omega) E_{\text{THz}}(\omega) e^{i\omega t}. \quad (4)$$

The time-dependent conductance  $g(t)$  is given by

$$g(t) = \int^t dt' I_g(t') (1 - e^{-(t-t')/\tau_C}) e^{-(t-t')/\tau_R} \quad (5)$$

where  $I_g(t)$  is the temporal intensity profile of the gating pulse and  $E_{\text{THz}}(\omega)$  is the Fourier transform of the incoming THz electric field  $e_{\text{THz}}(t)$ . The finite photocurrent rise time and the current recovery time are represented by  $\tau_C$  and  $\tau_R$ , respectively [32]. The response function  $H(\omega)$  represents the frequency-dependent ratio of the voltage induced at the sampling gap to the incident THz electric field spectral amplitude  $E_{\text{THz}}(\omega)$ , where  $e_{\text{THz}}(t)$  and  $E_{\text{THz}}(\omega)$  are assumed to approximate a plane wave at the receiver.  $H(\omega)$  depends on the coupling of the incident wave onto the antenna as well as the impedance matching conditions between the antenna and the transmission line in which it is embedded; both of these factors may be frequency-dependent.

The frequency response can be understood with the simple circuit diagram shown in Fig. 3 where the receiving antenna is represented by an equivalent open-circuit voltage source  $V_{oc}(\omega)$  and a series impedance  $Z_A(\omega)$  connected to an external circuit with impedance  $Z_0(\omega)$  [33]. From the reciprocity theorem,  $Z_A(\omega)$  is identical to the antenna impedance calculated when the same antenna is used as a transmitter [34]. The induced open-circuit voltage of the antenna  $V_{oc}(\omega)$  can be calculated from [35]

$$V_{oc}(\omega) = -\frac{1}{I_m} \int i_T(\omega, s) \mathbf{E}_{\text{THz}}(\omega, s) \cdot d\mathbf{s} \quad (6)$$

where  $i_T(\omega, s)$  is the current that would flow in the antenna at  $s$  if it were used as a transmitter,  $\mathbf{E}_{\text{THz}}(\omega, s)$  is the electric field of the incoming THz wave at  $s$ , and the integral is over the antenna surface.  $I_m$  is a normalization factor which represents the maximum of  $i_T$ . It should be noted that  $\mathbf{E}_{\text{THz}}(\omega, s)$  is the field which would exist at  $s$  when the receiver is not present. In other words,  $\mathbf{E}_{\text{THz}}(\omega, s)$  represents the incident field without taking into account any perturbations due to the presence of the receiver. When the overall size of the dipole is much less than the beam size of THz radiation, the electric field  $\mathbf{E}_{\text{THz}}(\omega, s)$  can be approximated as  $\mathbf{E}_{\text{THz}}(\omega)$  (for any given  $\omega$ ) because  $\mathbf{E}_{\text{THz}}(\omega, s)$  is spatially

uniform across the antenna. This will be true when the antenna dimensions are small compared to the THz wavelength of interest or, less restrictively, when the transmitter–receiver pair satisfies the far-field criterion. Specializing now to the dipole antennas studied in our experiments, when the dipole length is much shorter than the wavelength of the THz,  $i_T(\omega, s)$  is also frequency-independent. For example,  $i_T$  has a triangular profile for a short center-fed dipole [34]. In this case,  $V_{oc}$  can be approximated by  $E_{\text{THz}}(\omega)$  multiplied by a frequency-independent normalization factor  $C$  as

$$V_{oc}(\omega) = CE_{\text{THz}}(\omega). \quad (7)$$

In GaAs ( $n \sim 3$ ), frequencies of 1 and 2 THz correspond to wavelengths of 80 and 40  $\mu\text{m}$ , respectively. Therefore, the short dipole approximation becomes questionable for frequencies approaching 2 THz and above. But, since the relatively long carrier lifetime effectively performs low-pass filtering in PC detection, our PC detection is not sensitive in that frequency region. The actual voltage across the gap  $V_g$ , when there is a transmission line feed connected to the antenna, can be calculated from the following voltage divider expression:

$$V_g(\omega) = V_{oc}(\omega) \frac{Z_0(\omega)}{Z_0(\omega) + Z_A(\omega)} \quad (8)$$

where  $Z_0(\omega)$  and  $Z_A(\omega)$  are the impedances of the transmission line (plus load, if any) and the antenna, respectively. The radiation impedance of our short dipole is small in the frequency region of interest between tens of gigahertz and 2 THz [34]. (At very low frequency, the antenna reactance becomes large [36] and this leads to a zero dc response.) On the other hand, when  $Z_A$  is small compared to  $Z_0$ ,  $V_g$  can be approximated by  $V_{oc}$ . Therefore, if the measurement is limited to the THz range where the wavelength is much longer than the antenna length, both the open-circuit voltage and the voltage divider effect are nearly frequency-independent. As a result, we have

$$H(\omega) = 1. \quad (9)$$

When an antenna is longer, the impedance of antenna and transmission line can be matched at a certain frequency. This kind of resonance characteristic was reported by Smith *et al.* [2]. Our formalism is valid under the assumption that the resistance of the gap region upon illumination remains large compared to  $Z_A$ . Otherwise, the time-dependent gap resistance induced through the sampling action perturbs the voltage divider relation in a way that is not included in (8). Although this assumption may be only partially correct under our experimental conditions, nevertheless, based on our results in Section III, which show good agreement between theory and experiment, it appears that our formalism still accounts for impedance matching satisfactorily.

The frequency-independent open-circuit voltage relationship of (7) can be derived in an alternative way, also using the reciprocity theorem, as follows. By definition,  $V_{oc}(\omega)$  is independent of the external circuit connected to the antenna. Therefore, when we calculate  $V_{oc}$ , we can use any load at our convenience. When the antenna is connected to a load which satisfies the impedance-matching condition between the load and the antenna,  $Z_A(\omega) = Z_0^*(\omega)$ , for a particular frequency

$\omega$  of interest, the power  $W_r$  delivered to the load from the transmitter can be represented by [33]

$$W_r = \frac{\lambda^2 g_{dr} g_{dt}}{(4\pi r)^2} W_t \quad (10)$$

where  $W_t$  is the transmitted power,  $r$  is the distance between the transmitter and receiver, and  $g_{dr}$  and  $g_{dt}$  are the directional gains of the receiver and transmitter, respectively. In (10),  $W_t (g_{dt}/4\pi r^2)$  can be identified as the incident THz intensity at frequency  $\omega$ ,  $I_{\text{inc}}(\omega) = |E_{\text{THz}}(\omega)|^2/(2\eta)$ , at the detector, where  $\eta$  is the impedance of free space. Then, (10) can be rewritten as

$$W_r = \frac{\lambda^2 g_{dr}}{4\pi} \frac{|E_{\text{THz}}(\omega)|^2}{2\eta}. \quad (11)$$

On the other hand, the average power delivered to the matched load can be expressed in terms of  $V_{\text{oc}}$  as

$$W_r = \frac{1}{8} \frac{|V_{\text{oc}}|^2}{R_r} \quad (12)$$

where  $R_r = \text{Real}(Z_A)$  is the radiation resistance of the receiving antenna (which is the same as the radiation resistance of the same antenna used as a transmitter). By equating (12) and (11), we obtain

$$|V_{\text{oc}}|^2 = \frac{2\lambda^2}{\pi} g_{dr} R_r \frac{|E_{\text{THz}}(\omega)|^2}{2\eta}. \quad (13)$$

If we know the directional gain  $g_{dr}(\omega)$  and radiation resistance  $R_r(\omega)$  of the receiver, we can get the response function which relates the open-circuit voltage  $V_{\text{oc}}$  to the incoming THz electric field  $E_{\text{THz}}$ . For a short dipole,  $g_{dr} = 3/2$  and  $R_r = 10\pi^2(l/\lambda)^2$ , where  $l$  is the length of the dipole [34]. By substituting these expressions into (13), we obtain

$$|V_{\text{oc}}(\omega)|^2 = \frac{30\pi l^2}{\eta} |E_{\text{THz}}(\omega)|^2. \quad (14)$$

We find the open-circuit voltage  $V_{\text{oc}}(\omega)$  is proportional to the length of the antenna and to the incident electric field spectral amplitude  $E_{\text{THz}}(\omega)$  with a frequency-independent multiplication factor. In real experiments, the external circuit is not a matched load as in this hypothetical experiment; therefore, the actual voltage coupled across the gap  $V_g(\omega)$  still depends on  $V_{\text{oc}}(\omega)$  through the impedance-matching condition of (8).

As reported in the following, our experiments on a short dipole antenna without a substrate lens confirm the flat frequency response shown above ( $H(\omega) = 1$ ), i.e.,  $v_g(t)$  is directly proportional to the incoming electric field profile. This is in marked contrast to the well-known  $j\omega$  frequency dependence of a short dipole transmitting antenna.

When antennas are used with other coupling elements, the response function of the antenna reflecting those elements, should be used. An example of such a coupling element for microwave frequencies is the paraboloidal antenna. In that system, the electromagnetic wave is collected by a large aperture paraboloid and delivered to the active sensing unit which is located at the focal point of the paraboloid. The PC dipole THz antenna is often used with a hyper-hemispherical

substrate lens. In this case, the aperture of the entire THz system, consisting of the lens–dipole combination, is not shorter than the THz wavelength and may not be shorter than the THz beam size; the assumptions of the previous paragraphs used to derive the frequency-independent response function  $H(\omega) = 1$  may not be valid. In fact, we find that a short dipole receiver with a substrate lens does give rise to a frequency-dependent response  $H(\omega) \sim j\omega$  in the specific optical system and frequency range of our experiments. This will be covered in detail in Section III-C.

### III. RESULTS

#### A. Comparison of FS-EOS and PC-Sampled Waveforms

In this section, we compare the THz waveforms measured by FS-EOS and PC sampling and show that the waveforms measured by these techniques can be related by simple formulas already given as (3)–(5) [25]. Our approach is to use the waveforms measured by FS-EOS as the actual electric field waveform  $e_{\text{THz}}(t)$  in (3)–(5) in order to predict the PC-sampled waveforms. Since the PC-sampled waveforms and the FS-EOS waveforms are measured at the same position, we do not need to know the transfer function of the THz pulse from emitter to detector, which would be the same for both waveforms. This is in contrast to the situation where the THz waveforms measured by PC sampling are modeled based on the calculations of the field at the emitter [37]. Our approach allows for a quantitative investigation of the influence of the antenna response function and the photocurrent lifetime on the PC receiver operation. For the data of this section and Section III-B, the PC sampling was performed without a silicon lens to observe the pure PC antenna response. In Section III-C, we present the data obtained using a silicon substrate lens attached to a PC antenna and compare those with the ones obtained without a lens.

We performed FS-EOS and PC sampling experiments in the setups similar to Figs. 1 and 2. We performed our experiments in the back-to-back configuration, in which emitters and detectors were placed  $\sim 12$  cm apart and facing each other without any collimation optics involved in the beam path. This configuration was used in order to avoid any potential pulse reshaping in the use of THz collection optics such as paraboloidal mirrors. In each case, the receiver (either FS-EOS or PC sampling) was placed at the same position relative to the THz source.

We performed our comparison for three different sources of THz radiation, namely, two different biased large-aperture GaAs emitters and an unbiased ZnTe large-aperture emitter. These three emitters generated very distinct waveforms, which helped to confirm the validity of our theory. The biased emitters were fabricated by deposition of 3-mm spaced parallel electrodes either on a semi-insulating GaAs (SI-GaAs) or an LT-GaAs layer grown on SI-GaAs [31]. The LT-GaAs layer was grown at 280 °C and subsequently annealed by rapid thermal annealing at 575 °C for 30 s. We used a very thick (2.8  $\mu\text{m}$ ) LT-GaAs layer in order to minimize the partial transmission of the excitation pulse into the SI-GaAs substrate.

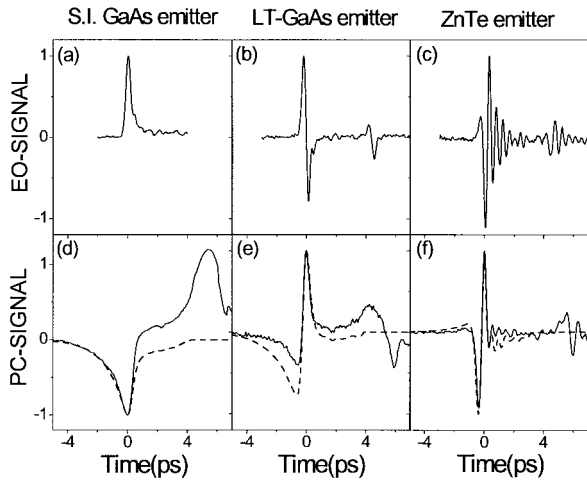


Fig. 4. Measured and calculated THz waveforms using FS-EOS and PC sampling. (a)–(c) FS-EOS measured waveforms. (d)–(f) PC-sampled waveforms (measurement: solid line; calculation: dashed line). The PC receiver was a short dipole fabricated on LT-GaAs annealed at 600 °C. No substrate lens was used in the PC sampling.

Typical biases were 200 V and 300 V for the SI-GaAs and LT-GaAs emitters, respectively. The unbiased ZnTe emitter was  $\langle 1\bar{1}0 \rangle$ -oriented and 1 mm thick. In the biased emitters, THz radiation is generated due to current surges, and the far-field radiation on the axis is given by the time derivative of the photogenerated current. In the unbiased ZnTe emitters, optical rectification, which is a second-order nonlinear process, is responsible for the THz generation [38].

For the FS-EOS receiver, we used a 150- $\mu\text{m}$ -thick ZnTe crystal with balanced detection. We used a relatively thin sensor crystal to minimize the waveform distortion by phonon–polariton coupling and GVM, which were described earlier. For the PC antenna receiver, we used a 50- $\mu\text{m}$ -long dipole antenna with a 5- $\mu\text{m}$  gap embedded in a 50- $\mu\text{m}$  spaced coplanar transmission line [6] and fabricated on the LT-GaAs layer. The LT-GaAs layer was grown at the same time as the emitter material. Most experiments were performed with the LT-GaAs layer annealed at 600 °C. A mode-locked Ti:sapphire laser with  $\sim 100$ -fs pulsewidth was used to provide pump and time-delayed probe pulses. The delay between the pump and probe was scanned using a computer-controlled stepper motor stage. The pump power was 800 mW for all cases, and the probe power was 2 mW for FS-EOS and 20 mW for PC sampling. The pump beam was collimated with a diameter of 1 mm. Of the 12 cm of the THz beam path, 10 cm was enclosed in a  $\text{N}_2$  purging box in order to reduce the effect of water vapor. Numerical calculations based on the diffraction integral show that, with this pump beam size and emitter detector separation, we are measuring the radiated field in the far-field region. This was further confirmed experimentally by the observation that, when we moved the emitter up to 80 cm away from detector, there was almost no change in the shape of the waveforms. This issue will be covered in more detail in Section III-E.

Fig. 4(a)–(c) shows the THz waveforms measured by FS-EOS. We can clearly see the difference between the waveforms from different emitters. From the SI-GaAs emitter, we obtained

an almost unipolar waveform, which is in sharp contrast to the bipolar waveform obtained from the LT-GaAs emitter. This was expected from the lifetime of photogenerated electrons in these materials. For PC antennas, far-field radiation can be represented by the time derivative of current profile in the emitter. Since the lifetime of the carriers is very long ( $>100$  ps) compared to the fast generation and acceleration of carriers ( $\ll 1$  ps) in the SI-GaAs, SI-GaAs has a step-like current profile, which gives almost unipolar waveforms. Note that if the detection sensitivity were sufficiently high we should see a very weak and long negative tail after the sharp positive peak from the slow decay of carrier population; if the scanning window is wide enough, the positive and negative areas will cancel each other, and there will be no dc component. LT-GaAs has a very short carrier lifetime; therefore, both rising and falling edges of the current profile generate a strong THz field, resulting in bipolar waveforms. The waveform from the ZnTe emitter has a strong ringing associated with the main oscillation. This ringing seems to be from the emitter, not from the sensor. When we changed to a 1-mm-thick sensor, the ringing remained almost the same, while, when we changed to a 150- $\mu\text{m}$  emitter with the default 150- $\mu\text{m}$  sensor, the ringing almost disappeared. We also performed FS-EOS for other emitters with the 1-mm-thick sensor; again, the waveforms are a little bit broadened but quite similar to the ones measured by the 150- $\mu\text{m}$ -thick crystal. These observations justify our assumption that the FS-EOS measurements with the thin sensor crystal provide a good measure of the actual THz waveform incident on the receiver.

Fig. 4(d)–(f) shows the corresponding waveforms measured by PC sampling (solid lines). Note that no substrate lens was used for these PC-sampling measurements. In each case, the shapes of the PC sampling and the corresponding FS-EOS waveforms are markedly different. Fig. 4(d)–(f) also show the predicted PC-sampling waveforms (dotted lines), which were calculated based on (3)–(5) using the FS-EOS data as the incident THz field  $e_{\text{THz}}(t) = \int d\omega e^{i\omega t} E_{\text{THz}}(\omega)$ . As fitting parameters, we used a carrier lifetime  $\tau_R = 1.3$  ps (in reasonable agreement with optical pump/probe time-resolved reflection measurements and sliding contact PC-sampling measurements), and a momentum relaxation time  $\tau_C = 0.18$  ps. We used a flat antenna response function  $H(\omega) = 1$ , for which the derived and measured waveforms match fairly well. We used the same fitting parameters to calculate waveforms corresponding to each of the three THz emitters. In the data, the features 5–6 ps after the main peaks are from reflections which occur at different delays for FS-EOS and PC detectors due to different substrate thicknesses. (This was not accounted for in the simulation.) The initial dip before the main features of the PC waveforms is associated with the lifetime of the photogenerated carriers and is most clearly observed for the unipolar waveform from the SI-GaAs emitter. For the bipolar waveforms (LT-GaAs and ZnTe emitters), this effect is less pronounced, because the positive and negative portions of the waveform partially cancel out in the convolution in (3)–(5). The agreement between simulated and measured waveforms for all three emitters validates our approach for modeling the PC receiver response.

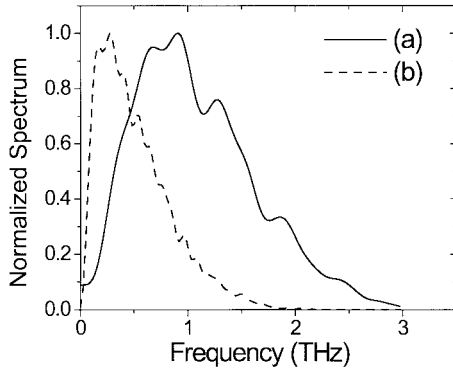


Fig. 5. Power spectra of THz waveforms from the LT-GaAs emitter measured by (a) FS-EOS (solid line) and (b) PC sampling (dashed line). The PC sampling was performed without an Si substrate lens.

Fig. 5 shows power spectra of the THz waveforms from the LT-GaAs emitter measured by (a) FS-EOS (solid line) and (b) PC sampling without an Si lens (dashed line). The FS-EOS measurement indicates a spectrum centered around 1 THz and extending to 3 THz, while the spectrum of the PC-sampled waveforms centers at 250 GHz and extends to 2 THz. This illustrates the bandwidth limitation arising due to the finite carrier lifetime of the receiver photoconductor. The observed bandwidth of the FS-EOS measured data is determined by the response of the PC-emitter, which in turn is determined by the carrier generation and acceleration and is not limited by the EO sampling process. The PC-sampled spectrum, on the other hand, is limited by the detection process.

### B. Effect of Carrier Lifetime on PC-Sampled Waveforms

Because of the gated nature of the PC-antenna used in this experiment, the time during which the antenna is open to measure the signal is determined by the convolution of the gate pulse profile and the lifetime of photogenerated carriers. Therefore, in order to measure fast transients, it is essential to have very short carrier lifetime and pulsewidth. Usually, the optical pulsewidth is very short compared to the carrier lifetime. Therefore, the carrier lifetime has more effect on the measured THz waveforms. In order to investigate the effect of carrier lifetime on the waveforms, we repeated the PC sampling with two detectors. These detectors were fabricated on LT-GaAs, grown at the same time and annealed at 600 °C and 625 °C, respectively. LT-GaAs has a characteristic that materials annealed at a higher temperature exhibit longer carrier lifetime [39]. According to our optical pump/probe measurement, the lifetimes are approximately 1.3 and 1.6 ps, respectively. The emitter was the same biased LT-GaAs large-aperture photoconductor (575 °C anneal) as in the previous section. Fig. 6(a) shows the results of the comparison. As expected, the negative dip before the main feature is broadened with the detector annealed at a higher temperature. Surprisingly, the main feature itself does not change with anneal temperature. This behavior is compared with the calculation in Fig. 6(b), in which calculated waveforms from PC detectors of different carrier lifetimes were plotted. We can observe good agreement between Fig. 6(a) and (b). The inset in Fig. 6 shows the hypothetical input THz waveform used to calculate

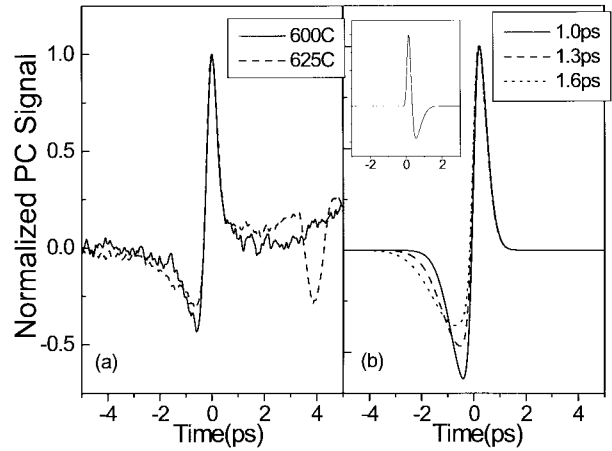


Fig. 6. Measured and simulated THz waveforms by PC detectors fabricated on materials having different carrier lifetimes. (a) Measurement. (b) Simulation using the input THz waveform shown in the inset.

the measured waveforms. This comparison demonstrates the character of the distortion of the waveform introduced by long lifetime detector material. This distortion results from the convolution of the time-dependent conductivity and the THz electric field. The conductivity profile is asymmetric in nature because of the fast rise time comparable to the optical pulsewidth and the slower decay time from carrier trapping/recombination. When this conductivity profile is convolved with bipolar waveforms, the first half cycle is greatly reduced while the latter half is less affected, leading to the above observations. In order to preserve the shape of the waveform, the photoconductive decay time should be much shorter than a half period of the THz waveform (which is not the case in our experiments!).

### C. The Effect of a Hyper-Hemispherical Lens on the PC-Sampled Waveform

For practical THz systems, the PC antenna is usually used together with a substrate lens in order to increase the coupling of the THz energy to the antenna [6]. The effect of such lenses on the waveforms has been discussed by several authors [6], [13], [37]. We have repeated our PC-sampling experiments with a hyper-hemispherical silicon lens attached to the PC antenna. The PC antenna receiver was a dipole fabricated on LT-GaAs annealed at 600 °C (the same one as in Section III-A). The diameter and the tip-to-bottom distance of the silicon lens were 10 mm and 6.5 mm, respectively, and the thickness of the GaAs PC receiver chip was 0.63 mm. This design is similar to that used in [40].

The results of the measurements are shown in Fig. 7. We can see distinct differences between the waveforms in Fig. 7 and the corresponding PC waveforms in Fig. 4. Besides the waveform changes, the amplitude of the THz signal was enhanced by more than a factor of 10 by using the silicon lens. Also shown in Fig. 7 are calculated PC waveforms (dotted lines) derived from the FS-EOS data, with the same  $\tau_R$  and  $\tau_C$  as used for the modeling results in Fig. 4. However, now we use an antenna response function  $H(\omega) = j\omega$ , which gives excellent agreement with the data waveforms. Agreement was

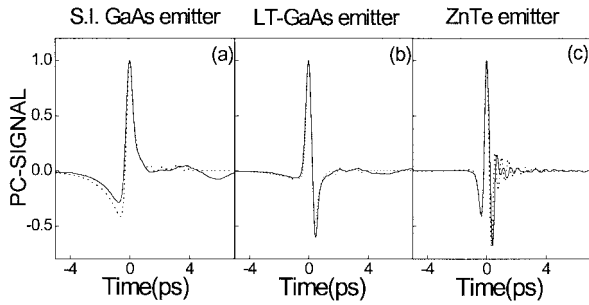


Fig. 7. Experimental and simulated THz waveforms from PC sampling with a silicon lens. The reflection features from the FS-EOS data were numerically eliminated before being used in the simulation. Measurement: solid line; calculation: dotted line.

not obtained for flat antenna response  $H(\omega) = 1$ . The  $j\omega$  factor leads to a derivative-like behavior in the time domain. Our results may be understood as follows. In our back-to-back configuration with 12-cm spacing, the THz beam at the receiver chip is larger than silicon lens aperture for all the frequencies where our PC receiver has significant frequency response. For example, using the diffraction integral, we calculate beam diameters (at the  $e^{-1}$  points of the field) of 29 and 15 mm for 1 and 2 THz, respectively. Therefore, the aperture is defined by the lens diameter and is approximately frequency-independent, resulting in a focused THz spot size which is inversely proportional to frequency. This smaller spot size for higher frequency components leads to a higher electric field amplitude for higher frequency, which results in a  $j\omega$  frequency factor. In order for this  $j\omega$  factor to be observed, the smallest spot size should be larger than the dipole antenna; in our case, this condition is easily satisfied. It is interesting to note that the condition that the beam size is larger than the silicon lens is approximately equivalent to the far-field criterion of the emitter/detector system including the silicon lens aperture. It is also important to note that observation of this effect depends on the specific THz optical system and frequency range. Grischkowsky *et al.* observed similar time-derivative behavior for a different THz optical system employing a pair of paraboloidal relay mirrors [6]. In that study, the THz beam size at the receiver was frequency-independent and smaller than the substrate lens aperture; as a result, the focused spot was again inversely proportional to frequency, but for a different reason.

#### D. Comparison of FS-EOS and PC-Sampled Waveforms with Optical Pulse Doublet Excitation

In Section III-A, in order to test the validity of our theory, we used three different emitters which generated distinct waveforms. Another way of generating different THz waveforms is using an optical pulse shaper. In previous experiments, shaped optical pulses, derived either through femtosecond optical pulse shaping [41], [42], or through chirped pulse interference [43], were used to excite PC dipole antennas in order to control the emitted THz waveforms. Here, in order to further test our theory, we compare PC and FS-EOS measurements of such shaped THz waveforms. Specifically, we used doublets generated by a femtosecond optical pulse shaper [44], [45]

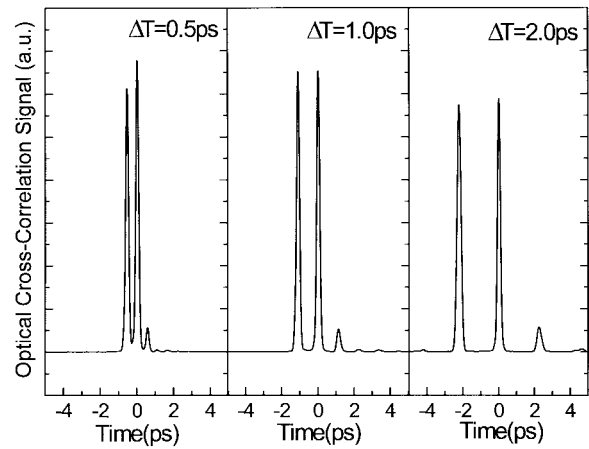


Fig. 8. Intensity cross correlations of the optical pulse doublets generated by a femtosecond optical pulse shaper.

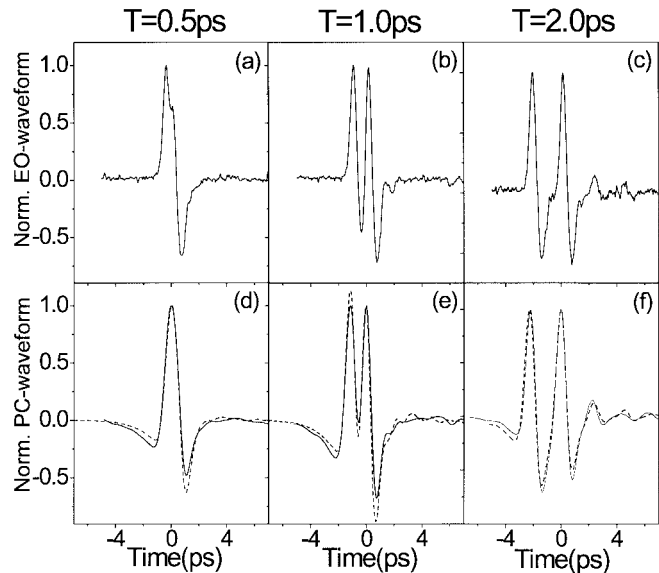


Fig. 9. FS-EOS and PC-sampled THz waveforms excited by optical doublets. The emitter was a LT-GaAs large-aperture biased photoconductor, and the PC antenna was used with a hyper-hemispherical silicon lens. (a)–(c) EO-sampled waveforms. (d)–(f) PC-sampled waveforms. Measurement: solid line; calculation: dotted line.

to excite a large-aperture THz emitter. The pulse shaper contained a liquid crystal modulator (LCM) array [45], [46] capable of both phase and amplitude modulation [46], which allowed the excitation pulse shapes to be programmed in real time under computer control. Fig. 8 shows three examples of optical cross correlations of the shaped doublet pulses used in our current experiments.

Fig. 9 shows the result of doublet excitation experiments performed with the LT-GaAs emitter annealed at 575 °C. The PC detector was on the LT-GaAs annealed at 600 °C, and an Si substrate lens was used. For a doublet spacing of  $\delta T = 0.5$  ps, we have almost a single THz pulse within the resolution of our measurements. From the FS-EOS measurement, we could get a small sign of two-pulse excitation; however, the THz generation process at the emitter itself is too slow to make any more significant signature. From PC sampling, no sign

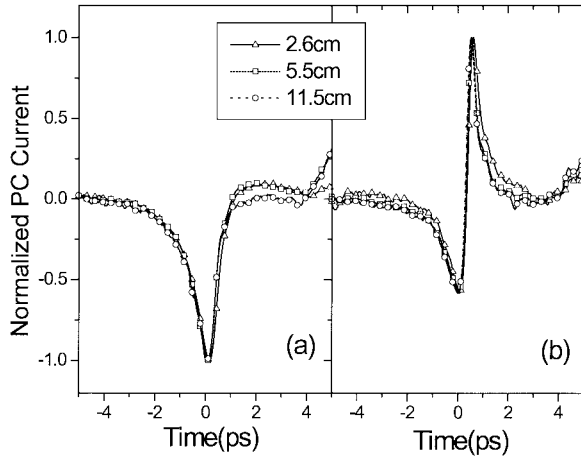


Fig. 10. THz waveforms measured at several distances from the emitter. Detector: PC detector without a silicon lens. (a) SI-GaAs large-aperture PC emitter. (b) LT-GaAs large-aperture PC emitter.

of doublet excitation is apparent except for some broadening of the waveform. But, as the spacing is increased to 1.0 and 2.0 ps, the THz radiation from each pulse is resolved. When the spacing is 2.0 ps, the two are completely separated from each other in the FS-EOS measurement, whereas in the PC-sampling measurement they are still coupled. In all cases, the match between the measured PC waveforms and the simulated PC waveforms using the FS-EOS data for the incident THz wave is very good, using the same set of parameters as before.

#### E. Near-Field Effects in Measurement of Wide-Band THz Radiation

Lastly, we measured THz waveforms varying the distance between the emitter and detector. We performed PC detection both with and without the silicon lens as well as FS-EOS, again all in the back-to-back configuration. We used large-aperture PC emitters fabricated from LT-GaAs annealed at 575 °C and from SI-GaAs, with an excitation beam diameter of 1 mm. The PC detector was a dipole fabricated on the LT-GaAs annealed at 600 °C. For these experiments, we fixed the location of the detector and changed the separation of the emitter from the detector. Because the optical pump beam and the THz beam are collinear, and assuming the same propagation velocity of THz and optical frequencies in air, we could maintain the same timing condition even while changing the emitter–detector distance. This is important when comparing the timing between waveforms later. Fig. 10 shows the THz waveforms from (a) LT-GaAs and (b) SI-GaAs emitters, both measured without a silicon lens. We find that, for each emitter, all the waveforms, which were measured at distances varying from 2.6 cm to 11.5 cm, are almost identical. Other data obtained at slightly different conditions (not shown) show that the waveforms are not changed out to 70 cm! Only the waveforms measured at 2.6-cm separation are perhaps very slightly broadened. However, in Fig. 11, where the THz waveforms from the LT-GaAs emitter were measured by PC detectors with a silicon lens attached, we see a completely different picture. The waveforms measured at shorter distance are much broader than the waveforms measured at longer

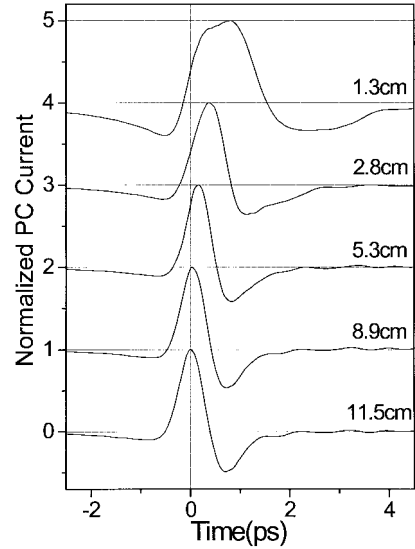


Fig. 11. THz waveforms measured at several distances from emitter. Detector: PC detector with a silicon lens. Emitter: large-aperture emitter on LT-GaAs annealed at 575 °C.

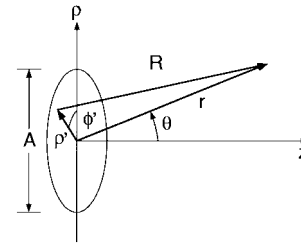


Fig. 12. Diagram showing the symbols used in the calculation of the electric field  $E$  at  $\mathbf{r}$  from the current distribution in the  $xy$  plane around the origin.  $A$  is the diameter of the emitter. This figure represents the case where the polar angle of the measurement point  $\phi = 0$ .

distances. Also, we found a delay in the arrival time of the THz wave for short emitter–receiver separations. However, the waveforms measured for separations greater than 9 cm are almost identical to each other and arrive at the same time.

This behavior can be understood from antenna theory (or diffraction theory). The electric field  $\mathbf{E}(\omega, \mathbf{r})$  radiated from an antenna with current distribution  $\mathbf{J}(\omega, \mathbf{r}')$  can be expressed by [33] (see Fig. 12)

$$\mathbf{E}(\omega, \mathbf{r}) = -j\omega\mu \int d\mathbf{r}' \frac{e^{ikR}}{4\pi R} \mathbf{J}(\omega, \mathbf{r}') \quad (15)$$

where  $R = |\mathbf{r} - \mathbf{r}'|$  is the distance from the source point to the measurement point,  $k = \omega/c$ , and the integration is over the antenna surface. Here the primed coordinates indicate the source coordinates. This formulation is valid where  $R > \lambda$ . When  $R < \lambda$ , the field is more static in nature and cannot be described as a radiating field. But since our measurement is concerned with very high frequency, where the lowest frequency of interest is  $\simeq 100$  GHz, this can be safely ignored for emitter–detector separations over  $\sim 1$  cm.

The distance  $R$  is given by

$$R = \sqrt{r^2 - 2\rho'r \sin\theta \cos(\phi' - \phi) + \rho'^2} \quad (16)$$

where  $r = \sqrt{x^2 + y^2 + z^2}$  is the distance of the measurement

point from the origin (center of the emitter),  $\rho' = \sqrt{x'^2 + y'^2}$  is the distance of the source point from the origin, and  $\phi$  and  $\phi'$  are polar angles of  $\mathbf{r}$  and  $\mathbf{r}'$ , respectively. Here we assume that the emitter surface is in the  $xy$  plane ( $z = 0$ ). When  $r$  is larger than the antenna radius  $A/2$ ,  $R$  can be expressed in a Taylor series using a binomial expansion

$$R = r - \rho' \sin \theta \cos(\phi - \phi') + \frac{\rho'^2}{2r}(1 - \sin^2 \theta \cos^2(\phi - \phi')) + \dots \quad (17)$$

The standard far-field approximation for (15) is that we replace  $R$  in the phase term  $jkR$  with  $r - \rho' \sin(\theta) \cos(\phi - \phi')$  and use  $R = r$  in the denominator. In this case, (15) can be simplified to

$$\mathbf{E}(\omega, \mathbf{r}) = -j\omega\mu \frac{e^{ikr}}{4\pi r} \int d\mathbf{r}' e^{-ik\rho' \sin \theta \cos(\phi - \phi')} \mathbf{J}(\omega, \mathbf{r}'). \quad (18)$$

In (18), the source term and propagation term are separated. For this far-field approximation to be valid, the criterion  $r > 2(A^2/\lambda)$  should be met which would allow maximum error of  $\pi/8$  for the phase term [34]. In this derivation, only the size of the emitter was considered. If both the emitter and detector have finite size,  $A_e$  and  $A_d$ , respectively,  $A = A_e + A_d$  should be used for the far-field criterion [34]. The above derivation was for the radiation of single-frequency  $\omega$ . When we apply this to wide-band radiation such as the THz of interest here, we should use the maximum frequency with appreciable amplitude. If the maximum frequency satisfies the far-field criterion, the lower frequency components automatically satisfy the criterion. Now we can calculate the  $R_{\text{farfield}} = 2(A^2/\lambda)$  for our THz detection system. For the PC detector without a silicon lens, the size of the dipole antenna detector (50  $\mu\text{m}$ ) is negligible compared to the size of the emitter aperture (1 mm). In this case, the  $R_{\text{farfield}}$  is 13 mm for 2 THz and 7 mm for 1 THz, which are small compared to all the observation distances. This is consistent with the data of Fig. 10, which shows the THz waveforms independent of distance over the range  $>2.6$  cm investigated. But when the silicon lens was used with the PC detector, the detector aperture size is increased. Fattinger *et al.* [47] and Jepsen *et al.* [37] have investigated beam propagation in similar systems. It is difficult to assign an effective aperture size exactly due to partial reflections and the inhomogeneous field distribution. If we use 5 mm (which is half the diameter of the lens) as the combined effective aperture size of the system, we get  $R_{\text{farfield}} = 33$  cm for 2 THz and 16 cm for 1 THz. This agrees roughly with our observation (Fig. 11) that the waveform did not change appreciably for propagation over distances  $\geq 10$  cm. The broadening and additional delay of THz waveforms at shorter observation distances arise because the distances the THz wave components must travel depends on the particular points in the emitter and detector. The delay can be estimated by simple trigonometry. For the center-to-center distance between the emitter and the detector  $r$ , and the combined aperture size  $A$ , the maximum extra time delay  $\Delta T$ , is given by  $\Delta T = (\sqrt{r^2 + (A/2)^2} - r)/c$ . For example, if we use  $r = 3$  cm and  $A = 5$  mm for our PC detector with a silicon lens, we get  $\Delta T = 0.35$  ps. The THz waveform measured at a distance of 2.8 cm in Fig. 11 shows that the

peak is displaced by 0.5 ps compared to the far-field data, again in qualitative agreement with our simple estimate.

We also performed distance dependence experiments with FS-EOS with emitter–receiver separations between 12–28 cm. Because of the presence of the pellicle beamsplitter, we could not make the distance shorter. In the range investigated, we did not observe any change of pulse shape, other than the attenuation at larger distance.

Near-field effects have been studied experimentally [48], [49] or theoretically [50] by a number of groups. Among those, the experiments of Budiarto *et al.* are most similar to our work. But, in those experiments, a SI-GaAs PC emitter with a very large aperture (3 cm) was used, and all the experiments were limited to the near-field region.

Our experiments clearly demonstrate the existence of a far-field region even for wide-band THz radiation. When each frequency component satisfies the far-field condition—when the highest frequency component satisfies this, the others do automatically—the spectral amplitude of each frequency component is governed by an  $1/r$  scaling rule, so that each frequency is attenuated at the same rate, as seen in (18). Beyond the minimum separation needed to satisfy the far-field criterion, the THz waveform and its frequency dependence become independent of the emitter–detector distance  $r$ .

#### IV. CONCLUSION

We have analyzed THz waveforms measured by FS-EOS and PC sampling and have directly compared the THz radiation waveforms measured from FS-EOS and PC-sampling receivers. Although we observed significant differences between the two types of measurements, we demonstrated that the waveforms measured by the PC antenna can be derived from the FS-EOS waveforms by using a simple theoretical formalism which takes into account the response of the PC antenna and the photocarrier lifetime. For a PC THz receiver consisting of a short dipole without a substrate lens, we showed both experimentally and theoretically that the receiver antenna response is approximately flat over the THz frequency range of interest. For the same receiver with a substrate lens, we found a  $j\omega$  frequency dependence for the receiver's antenna response, which we explained based on the specific optical system in use. Our results help to elucidate the role of the frequency-dependent antenna response in PC-sampling THz receivers. We also investigated the effect of the PC carrier lifetime on the THz waveform measurement and explained our results through simulation. Finally, we demonstrated near-field effects in PC-sampling measurements of THz waveforms and explored the evolution of the THz radiation from the near-field into the far-field region.

#### ACKNOWLEDGMENT

The authors acknowledge helpful discussions with Dr. X.-C. Zhang.

#### REFERENCES

- [1] D. H. Auston, K. P. Cheung, and P. R. Smith, "Picosecond photoconducting Hertzian dipoles," *Appl. Phys. Lett.*, vol. 45, pp. 284–286, 1984.

- [2] P. R. Smith, D. H. Auston, and M. C. Nuss, "Subpicosecond photoconductive dipole antennas," *IEEE J. Quantum Electron.*, vol. 24, pp. 255–260, 1988.
- [3] X.-C. Zhang, B. B. Hu, J. T. Darrow, and D. H. Auston, "Generation of femtosecond electromagnetic pulses from semiconductor surfaces," *Appl. Phys. Lett.*, vol. 56, pp. 1011–1013, 1990.
- [4] N. M. Froberg, B. B. Hu, X.-C. Zhang, and D. H. Auston, "Terahertz radiation from a photoconductive antenna arrays," *IEEE J. Quantum Electron.*, vol. 28, pp. 2291–2301, 1992.
- [5] B. B. Hu, A. S. Weling, D. H. Auston, A. V. Kuznetsov, and C. J. Stanton, "dc-electric-field dependence of THz radiation induced by femtosecond optical excitation of bulk GaAs," *Phys. Rev. B*, vol. 49, pp. 2234–2237, 1994.
- [6] M. van Exter, C. Fattinger, and D. Grischkowsky, "High-brightness terahertz beams characterized with an ultrafast detector," *Appl. Phys. Lett.*, vol. 55, pp. 337–339, 1989.
- [7] D. R. Grischkowsky, M. B. Ketchen, C.-C. Chi, I. I. N. Duling, N. J. Halas, J.-M. Halbout, and P. G. May, "Capacitance free generation and detection of subpicosecond electrical pulses on coplanar transmission lines," *IEEE J. Quantum Electron.*, vol. 24, pp. 221–225, 1988.
- [8] C. Fattinger and D. R. Grischkowsky, "A Cherenkov source for freely-propagating terahertz beams," *IEEE J. Quantum Electron.*, vol. 25, pp. 2608–2610, 1989.
- [9] D. Grischkowsky, S. Keiding, M. van Exter, and C. Fattinger, "Far-infrared time-domain spectroscopy with terahertz beams of dielectrics and semiconductors," *J. Opt. Soc. Amer. B*, vol. 7, pp. 2006–2015, 1990.
- [10] M. C. Nuss, P. M. Mankiewich, M. L. O'Malley, and E. H. Westerman, "Dynamic conductivity and coherence peak in  $\text{YBa}_2\text{Cu}_3\text{O}_7$  superconductors," *Phys. Rev. Lett.*, vol. 66, pp. 3305–3308, 1991.
- [11] I. Brener, D. Dykaar, A. Frommer, L. N. Pfeiffer, J. Lopata, J. Wynn, K. West, and M. C. Nuss, "Terahertz emission from electric field singularities in biased semiconductors," *Opt. Lett.*, vol. 21, pp. 1924–1926, 1996.
- [12] B. B. Hu, E. A. de Souza, W. H. Knox, J. E. Cunningham, and M. C. Nuss, "Identifying the distinct phases of carrier transport in semiconductor with 10 fs resolution," *Phys. Rev. Lett.*, vol. 74, pp. 1689–1691, 1995.
- [13] D. M. Mittleman, R. H. Jacobsen, and M. C. Nuss, "T-ray imaging," *J. Select. Topics Quantum Electron.*, vol. 2, pp. 679–692, 1996.
- [14] R. A. Cheville and D. Grischkowsky, "Time domain terahertz impulse ranging studies," *Appl. Phys. Lett.*, vol. 67, pp. 1960–1962, 1995.
- [15] J. A. Valdmanis, G. Mourou, and C. W. Gabel, "Picosecond electro-optic sampling system," *Appl. Phys. Lett.*, vol. 41, pp. 211–212, 1982.
- [16] Q. Wu and X.-C. Zhang, "Free-space electro-optic sampling of terahertz beams," *Appl. Phys. Lett.*, vol. 67, pp. 3523–3525, 1995.
- [17] ———, "Ultrafast electro-optic field sensors," *Appl. Phys. Lett.*, vol. 68, pp. 1604–1606, 1996.
- [18] Q. Wu, M. Litz, and X.-C. Zhang, "Broadband detection capability of ZnTe electro-optic field detectors," *Appl. Phys. Lett.*, vol. 68, pp. 2924–2926, 1996.
- [19] Q. Wu, F. G. Sun, P. Campbell, and X.-C. Zhang, "Dynamic range of an electro-optic field sensor and its imaging applications," *Appl. Phys. Lett.*, vol. 68, pp. 3224–3226, 1996.
- [20] Q. Wu, T. D. Hewitt, and X.-C. Zhang, "Two-dimensional electro-optic imaging of THz beams," *Appl. Phys. Lett.*, vol. 69, pp. 1026–1028, 1996.
- [21] Q. Wu and X.-C. Zhang, "Design and characterization of traveling-wave electrooptic terahertz sensors," *J. Select. Topics Quantum Electron.*, vol. 2, pp. 693–700, 1996.
- [22] A. Nahata, D. H. Auston, T. F. Heinz, and C. Wu, "Coherent detection of freely propagating terahertz radiation by electro-optic sampling," *Appl. Phys. Lett.*, vol. 68, pp. 150–152, 1996.
- [23] A. Nahata, A. S. Weling, and T. F. Heinz, "A wideband coherent terahertz spectroscopy system using optical rectification and electro-optic sampling," *Appl. Phys. Lett.*, vol. 69, pp. 2321–2323, 1996.
- [24] Y. Cai, I. Brener, J. Lopata, J. Wynn, L. Pfeiffer, J. B. Stark, Q. Wu, X.-C. Zhang, and J. Federici, "Coherent terahertz radiation detection: Direct comparison between free space electro-optic sampling and antenna detection," *Appl. Phys. Lett.*, vol. 50, pp. 444–446, 1998.
- [25] S.-G. Park, M. R. Melloch, and A. M. Weiner, "Comparison of terahertz waveforms measured by electro-optic and photoconductive sampling," *Appl. Phys. Lett.*, vol. 73, pp. 3184–3186, 1998.
- [26] A. Yariv, *Quantum Electronics*, New York: Wiley, 1989.
- [27] H. J. Bakker, G. C. Cho, H. Kurz, Q. Wu, and X.-C. Zhang, "Distortion of terahertz pulses in electro-optic sampling," *J. Opt. Soc. Amer. B*, vol. 15, pp. 1795–1801, 1998.
- [28] P. R. Smith, D. H. Auston, A. M. Johnson, and W. M. Aug.yniak, "Picosecond photoconductivity in radiation-damaged silicon-on-sapphire films," *Appl. Phys. Lett.*, vol. 38, pp. 47–50, 1981.
- [29] S. Gupta, Y. Frankel, J. A. Valdmanis, J. F. Whitaker, G. A. Mourou, F. W. Smith, and A. R. Calawa, "Subpicosecond carrier lifetime in gas grown by molecular beam epitaxy at low temperatures," *Appl. Phys. Lett.*, vol. 59, pp. 3276–3278, 1991.
- [30] A. C. Warren, N. Katznellenbogen, D. Grischkowsky, J. M. Woodall, M. R. Melloch, and N. Otsuka, "Subpicosecond, freely propagating electromagnetic pulse generation and detection using GaAs:As epilayers," *Appl. Phys. Lett.*, vol. 58, pp. 1512–1514, 1991.
- [31] M. R. Melloch, D. D. Nolte, J. M. Woodall, J. C. P. Chang, D. B. Janes, and E. S. Harmon, "Molecular beam epitaxy of nonstoichiometric semiconductors and multiphase material system," *Crit. Rev. in Solid State and Mater. Sci.*, vol. 21, pp. 189–263, 1996.
- [32] D. Grischkowsky, "Nonlinear generation of subpicosecond pulses of THz electromagnetic radiation by optoelectronics—Application to time-domain spectroscopy," in *Frontiers in Nonlinear Optics*, H. Walther, N. Koroteev, and M. O. Scully, Eds. Philadelphia, PA: Inst. Physics, 1993, pp. 196–228.
- [33] S. Ramo, J. R. Whinnery, and T. van Duzer, *Fields and Waves in Communication Electronics*. New York: Wiley, 1984.
- [34] C. A. Balanis, *Antenna Theory*, New York: Wiley, 1982.
- [35] G. D. Monteth, *Applications of the Electromagnetic Reciprocity Principle*. Oxford, U.K.: Pergamon, 1973.
- [36] R. C. Hansen, "Fundamental limitations in antennas," *Proc. IEEE*, vol. 69, pp. 170–182, 1931.
- [37] P. U. Jepsen, R. H. Jacobsen, and S. R. Keiding, "Generation and detection of terahertz pulses from biased semiconductor antennas," *J. Opt. Soc. Amer. B*, vol. 13, pp. 2424–2436, 1996.
- [38] X.-C. Zhang, Y. Jin, and X. F. Ma, "Coherent measurement of THz optical rectification from electro-optic crystals," *Appl. Phys. Lett.*, vol. 61, pp. 2764–2766, 1992.
- [39] E. S. Harmon, M. R. Melloch, J. M. Woodall, D. D. Nolte, N. Otsuka, and C. L. Chang, "Carrier lifetime versus anneal in low temperature growth GaAs," *Appl. Phys. Lett.*, vol. 63, pp. 2248–2250, 1993.
- [40] M. van Exter and D. Grischkowsky, "Carrier dynamics of electrons and holes in moderately doped silicon," *Phys. Rev. B*, vol. 41, pp. 12140–12149, 1990.
- [41] Y. Liu, S.-G. Park, and A. M. Weiner, "Enhancement of narrow-band terahertz radiation from photoconductive antennas by optical pulse shaping," *Opt. Lett.*, vol. 21, pp. 1762–1764, 1996.
- [42] Y. Liu, S.-G. Park, and A. M. Weiner, "Terahertz waveform synthesis via optical pulse shaping," *J. Select. Topics Quantum Electron.*, vol. 2, pp. 709–719, 1996.
- [43] A. S. Weling and D. H. Auston, "Novel sources and detectors for coherent tunable narrow-band terahertz radiation in free space," *J. Opt. Soc. Amer. B*, vol. 13, pp. 2783–2791, 1996.
- [44] A. M. Weiner, J. P. Heritage, and E. M. Kirschner, "High-resolution femtosecond pulse shaping," *J. Opt. Soc. Amer. B*, vol. 5, pp. 1563–1572, 1988.
- [45] A. M. Weiner, D. E. Leaird, J. S. Patel, and J. R. Wullert, "Programmable femtosecond pulse shaping by use of a multielement liquid-crystal phase modulator," *Opt. Lett.*, vol. 15, pp. 326–328, 1990.
- [46] M. M. Wefers and K. A. Nelson, "Generation of high-fidelity programmable ultrafast optical waveforms," *Opt. Lett.*, vol. 20, pp. 1047–1049, 1995.
- [47] C. Fattinger and D. R. Grischkowsky, "Beams of terahertz electromagnetic pulses," in *OSA Proc. Picosecond Electronics and Optoelectronics*, 1989, pp. 225–231.
- [48] E. Budiarto, N. W. Pu, S. Jeong, and J. Bokor, "Near-field propagation of terahertz pulses from a largeaperture antenna," *Opt. Lett.*, vol. 23, pp. 213–215, 1998.
- [49] S. Hunsche, M. Koch, I. Brener, and M. C. Nuss, "THz near-field imaging," *Opt. Commun.*, vol. 150, pp. 22–26, 1998.
- [50] A. E. Kaplan, "Diffraction-induced transformation of near-cycle and subcycle pulses," *J. Opt. Soc. Amer. B*, vol. 15, pp. 951–956, 1998.

**Sang-Gyu Park**, photograph and biography not available at the time of publication.

**Michael R. Melloch** (S'76–M'76–SM'91), photograph and biography not available at the time of publication.

**Andrew M. Weiner** (S'84–M'84–M'91–F'95), photograph and biography not available at the time of publication.